



Originally published as:

Lüdtke, T., Wiedemann, D., Efthimiopoulos, I., Becker, N., Seidel, S., Janka, O., Pöttgen, R., Dronskowski, R., Koch-Müller, M., Lerch, M. (2017): HP-MoO<sub>2</sub>: A High-Pressure Polymorph of Molybdenum Dioxide. - *Inorganic Chemistry*, 56, 4, pp. 2321—2327.

DOI: <http://doi.org/10.1021/acs.inorgchem.6b03067>

# HP-MoO<sub>2</sub>—A New High-Pressure Polymorph of Molybdenum Dioxide

Tobias Lüdtké,<sup>a</sup> Dennis Wiedemann,<sup>a</sup> Ilias Efthimiopoulos,<sup>b</sup> Nils Becker,<sup>c</sup>  
Oliver Janka,<sup>d</sup> Rainer Pöttgen,<sup>d</sup> Richard Dronskowski,<sup>c,e</sup> Monika Koch-Müller\*<sup>b</sup>,  
Martin Lerch\*<sup>a</sup>

*a: Institut für Chemie, Technische Universität Berlin, Straße des 17. Juni 135, D-10623 Berlin, Germany*

*b: Deutsches GeoForschungsZentrum Potsdam, Telegrafenberg, D-14473 Potsdam, Germany*

*c: Institut für Anorganische Chemie, RWTH Aachen University, Landoltweg 1, D-52056 Aachen, Germany*

*d: Institut für Anorganische und Analytische Chemie, Universität Münster, Corrensstrasse 30, D-48149 Münster, Germany*

*e: Jülich-Aachen Research Alliance (JARA-HPC), RWTH Aachen University, D-52074 Aachen, Germany*

## Keywords

High pressure; molybdenum dioxide; single-crystal X-ray diffraction; Raman spectroscopy; density-functional theory computations; magnetism

## Abstract

High-pressure molybdenum dioxide (HP-MoO<sub>2</sub>) was synthesized using a multi-anvil press at 18 GPa and 1073 K, as motivated by previous first-principles calculations. The crystal structure was determined by single-crystal X-ray diffraction. The new polymorph crystallizes isotypically to HP-WO<sub>2</sub> in the orthorhombic crystal system in space group *Pnma* and was found to be diamagnetic. Theoretical investigations using structure optimization at density-functional theory (DFT) level indicate a transition pressure of 5 GPa at 0 K and identify the new compound as slightly metastable at ambient pressure with respect to the thermodynamically stable monoclinic MoO<sub>2</sub> ( $\alpha$ -MoO<sub>2</sub>;  $\Delta E_m = 2.2 \text{ kJ}\cdot\text{mol}^{-1}$ ).

## Introduction

Elements of the sixth group of the periodic table form compounds with the metal atom in many different oxidation states. Valence-isoelectronic molybdenum and tungsten have a similar chemistry in consequence of the almost identical ionic radii as one result of the lanthanide contraction. Many binary oxides are known for both elements, but only the di- and trioxides have the element in just one oxidation state (+IV / +VI).  $\text{MoO}_2^{1-5}$  and  $\text{WO}_2^{1,2,5}$  (from now on, we will call those compounds  $\alpha\text{-MoO}_2$  and  $\alpha\text{-WO}_2$ ) crystallize isotypically in the monoclinic space group  $P2_1/c$ .  $\text{MoO}_2$  is the eponym for this structure type, which can be described as a distorted rutile type. It is built of chains of  $\text{MO}_6$  polyhedra connected *via* opposite edges along the  $a$  axis with alternating distances between the metal atoms.<sup>5</sup> All vertices are connected with neighboring chains. The distortion is caused by a Peierls-type instability of the electronic structure.<sup>6</sup> Other oxides, like  $\alpha\text{-ReO}_2$  and a low-temperature form of  $\text{VO}_2$ , adopt the same structure type.<sup>3</sup> Reports on tetragonal rutile-type variants (space group  $P4_2/mnm$ ) of  $\alpha\text{-MoO}_2$  and  $\alpha\text{-WO}_2$ , one from 1926 by Goldschmidt *et al.*<sup>1</sup> and a second one regarding the molybdenum dioxide from 2004 by Seisenbaeva *et al.*,<sup>7</sup> are rare. Simulated diffraction patterns indicate that a very good instrumental resolution is necessary to distinguish between monoclinic and tetragonal rutile variants.<sup>8</sup> Additionally, it was proposed that a distorted rutile type, crystallizing in space group  $I4_1md$ , was the actual product in both reported cases. According to quantum-chemical computation, this variant is *ca.*  $7 \text{ kJ}\cdot\text{mol}^{-1}$  less stable than the monoclinic form of the dioxide.<sup>8</sup> Other theoretical studies regarding  $\alpha\text{-MoO}_2$  cover a wide range of various aspects.<sup>5,9-13</sup> It can be found in the mineral tugarinovite (named after the geochemist Alexsey Ivanovich Tugarinov)<sup>14</sup> and shows a metal-like electric conductivity being unusual for transition-metal oxides.<sup>15,16</sup> It does not have a variety of technological applications such as  $\text{MoO}_3$  but there are some interesting approaches for usage as anode material in lithium-ion batteries,<sup>15,17-20</sup> films for energy storage,<sup>21</sup> soft-magnetic and optical materials,<sup>22-24</sup> and as nanorods.<sup>22,25</sup>

The synthesis of other oxides with metal ions in just one oxidation state probably cannot be achieved by conventional chemical methods, like oxidation or reduction. Another approach to prepare new compounds is the usage of high pressure on existing binary oxides. High-pressure polymorphs are often characterized by a higher density and an increased coordination number of the atoms. For example, the cotunnite type with 9-fold coordinated cations is a common structure

type for high-pressure polymorphs of transition-metal oxides<sup>26,27</sup> and oxide nitrides.<sup>28</sup> The synthesis of an orthorhombic high-pressure polymorph of tungsten dioxide (HP-WO<sub>2</sub>) is possible at 8 GPa and 1120 K.<sup>29</sup> Remarkably, the crystal structure of this compound has been derived just using powder X-ray diffraction (XRD) data with very weak reflections dominated by the cation lattice. Up to now, only first-principle studies based on quantum-chemical computation at the density-functional theory (DFT) level have been published on a molybdenum analogue. Predicted by calculations, a metastable high-pressure polymorph with an orthorhombic rutile variant should be formed at around 25 GPa.<sup>8</sup> A monoclinic high-pressure polymorph of MoO<sub>3</sub> has been prepared using pressures greater than 6 GPa and temperatures greater than 973 K.<sup>30</sup> In the present work, we report on synthesis and characterization of a new high-pressure polymorph of molybdenum dioxide.

## Experimental

**Synthesis.** As starting material for the high pressure synthesis, we used  $\alpha$ -MoO<sub>2</sub>, which we had prepared by reduction of MoO<sub>3</sub> (Sigma Aldrich, 99.5%) in a tube furnace with direct gas feed at  $T = 858$  K for 18 h with flow rates of 15 L·h<sup>-1</sup> H<sub>2</sub> and 0.7 L·h<sup>-1</sup> O<sub>2</sub>. The samples were placed in platinum capsules, which had an outer diameter of 1.4 mm (wall thickness of 0.2 mm) and were 2 mm long. We performed the multi-anvil run (MA-497) with a 10/5 assembly, rhenium heater, and type C thermocouple at  $p = 18$  GPa and  $T = 1073$  K for 30 h. At the end of the run, the temperature was quenched to ambient conditions within 2 min and the decomposition time was 43 h to avoid breakage of the WC cubes. For more details about the pressure calibration, we refer to Koch-Müller *et al.*<sup>31</sup> After the experiment, the recovered capsule was filed open.

**X-Ray Diffraction.** A Rigaku R/AXIS200 SPIDER and a PANalytical X'Pert MPD Pro diffractometer were used for powder XRD measurements at ambient temperature. The diffractometers operate with unmonochromated Cu- $K_{\alpha}$  radiation ( $\lambda_1 = 154.060$  pm,  $\lambda_2 = 154.443$  pm,  $I(\lambda_2)/I(\lambda_1) = 0.500$ ) at 40 kV and 30 mA (Rigaku)/40 mA (PANalytical). Powder diffraction-pattern simulations, Rietveld refinements,<sup>32</sup> and Le Bail profile decompositions<sup>33</sup> were carried out using the program FULLPROF.<sup>34</sup> Starting values for the refinements were the fractional atomic coordinates and lattice parameters of HP-WO<sub>2</sub>.<sup>29</sup> Profiles were fitted with a pseudo-Voigt profile function. The following parameters were fitted in the Le Bail decomposition process: three unit-

cell parameters, one overall temperature displacement factor, three Gaussian half-width ( $U$ ,  $V$ ,  $W$ ) parameters, a mixing and one Lorentzian ( $\eta_0$ ,  $X$ ) parameter, two asymmetry parameters, displacement, and transparency. The background was fitted with 36 points with refinable heights.

Single-crystal diffraction data was collected at 150.0(1) K using an Agilent SuperNova diffractometer equipped with a goniometer in  $\kappa$  geometry, an “Atlas” CCD-detector, and a mirror-monochromated “Nova” Cu- $K_\alpha$  source ( $\lambda = 154.184$  pm). Diffraction images were integrated with CRYALISPRO.<sup>35</sup> An analytical numeric absorption correction using a multifaceted crystal model was performed.<sup>36</sup> The structure was solved with SHELXS-2013 using Direct Methods and refined with SHELXL-2016 against  $F_o^2$  data using the full-matrix least-squares algorithm.<sup>37</sup> All atoms were refined anisotropically. An extinction correction was performed as implemented in SHELXL-2016; the corresponding parameter refined to 0.0038(2). Structure graphics were produced using DIAMOND 3.2.<sup>38</sup>

Further details of the crystal structure investigations may be obtained from FIZ Karlsruhe, 76344 Eggenstein-Leopoldshafen, Germany (fax: +49 7247 808-666; e-mail: [crysdata@fiz-karlsruhe.de](mailto:crysdata@fiz-karlsruhe.de)), on quoting the deposition numbers CSD-432325.

**Raman Spectroscopy.** Raman spectra of unoriented crystallites were collected in the 100–1200  $\text{cm}^{-1}$  wavenumber range with a HORIBA Jobin Yvon LabRAM HR800 UV-VIS spectrometer, equipped with a 1800 grooves/mm grating and a CCD detector. The excitation wavelength was the Ar<sup>+</sup> laser line  $\lambda = 514.5$  nm with an incident laser power of 0.2 mW, whereas a 50 $\times$  lens was used for focusing on the sample surface. The acquisition time for each spectrum was 400 sec with 10 accumulations.

**Quantum-Chemical Calculations.** The quantum-chemical studies were based on previously published results<sup>8</sup> and supplemented with data acquired from the experiments discussed here. The Vienna *ab-initio* simulation package (VASP) was used to perform periodic DFT calculations.<sup>39</sup> Core and valence electrons were separated using projector-augmented waves (PAW).<sup>40</sup> The generalized-gradient approximation as described by Perdew, Burke, and Ernzerhof (GGA-PBE)<sup>41,42</sup> was used to treat the exchange and correlation contributions. As the initial calculations on MoO<sub>2</sub> were carried out with dispersion correction, the herein presented additional calculations also include the corrections for van-der-Waals forces, namely Grimme’s “D3(BJ)” dispersion correction with Becke–Johnson damping<sup>43,44</sup> as implemented in VASP 5.3.5. The energy-cutoff

was set to 500 eV and a  $k$ -point grid of  $12 \times 12 \times 12$  ( $\alpha$ -MoO<sub>2</sub>) or  $6 \times 7 \times 12$  (HP-MoO<sub>2</sub>) ensured well-converged structures. All atomic positions and lattice parameters were allowed to relax until the ionic convergence criterion of  $10^{-6}$  eV was reached. The high-pressure behavior was calculated by scaling the cell parameters from 94% to 104% (with fixed  $a:b:c$  ratio), and the resulting energy vs. volume data were fitted to the Birch–Murnaghan equation of state.<sup>45</sup> Thus, the pressure and, eventually, the reaction enthalpies as a function of the pressure were calculated. Additional thermodynamic properties were calculated using Phonopy.<sup>46</sup> As a first step, supercells of the optimized structures were constructed. All symmetry-inequivalent atoms were then slightly shifted out of their equilibrium positions to calculate the Hellmann–Feynman forces. Subsequently, the force constants and then the dynamical matrices were computed. Through combination of the eigenvalues (phonon wavenumbers) with Bose–Einstein statistics, the free phonon energy was obtained.<sup>47</sup> The thermodynamic properties at finite temperatures are straightforwardly accessible from these theoretical data.

**Magnetic Properties.** Hand-selected crystals of HP-MoO<sub>2</sub> were packed in a polyethylene (PE) capsule and attached to the sample holder rod of a vibrating sample magnetometer (VSM) unit for measuring the magnetization  $M(T)$  in a Quantum Design Physical Property Measurement System (PPMS). The sample was investigated in the temperature range of 3–300 K with magnetic flux densities of 10 and 50 kOe.

## Results and Discussion

Although molybdenum and tungsten show similar behavior, it is surprising that only the dioxide of tungsten is reported to form a high-pressure polymorph. Quantum-chemical calculations on DFT level were performed to investigate the high-pressure behavior of MoO<sub>2</sub> as described in the previous study on possible new polymorphs of MoO<sub>2</sub>.<sup>8</sup> Additionally, the high-pressure polymorph of tungsten dioxide (HP-WO<sub>2</sub>) was used as a starting structure for the optimization of MoO<sub>2</sub> and the following investigations. Our calculations reveal an isostructural high-pressure polymorph of MoO<sub>2</sub> based on HP-WO<sub>2</sub>. This phase is calculated to be only  $2.2 \text{ kJ} \cdot \text{mol}^{-1}$  less stable than  $\alpha$ -MoO<sub>2</sub> and should form at pressures above 5 GPa (**Figure 1**). A second polymorph, with a structure dubbed *ortho*-TiO<sub>2</sub> (for details see Ref. <sup>8</sup>), is predicted to form between 25 and 30 GPa. The calculated phonon density of states (PDOS) of HP-MoO<sub>2</sub> shows no

imaginary modes at ambient or the transition pressure (**Figure 2**) and can therefore be identified as a minimum of the potential energy surface. Based on these phonon calculations, we also provide a list of the calculated Raman-active modes in the **Supplement** for comparison with experiment. One should note that the calculated pressure is only valid at 0 K, so under experimental conditions with finite temperatures the transition pressure is likely to be different. Based on these theoretical findings, we continued with the corresponding high-pressure synthesis.

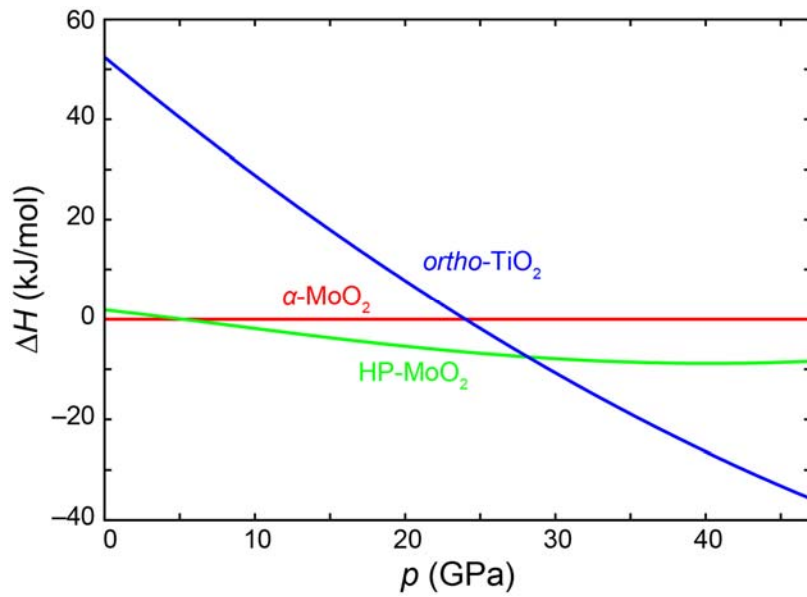


**Figure 1.** Theoretically calculated enthalpy of HP-MoO<sub>2</sub> and the other potential polymorph with *ortho*-TiO<sub>2</sub> structure relative to  $\alpha$ -MoO<sub>2</sub>.

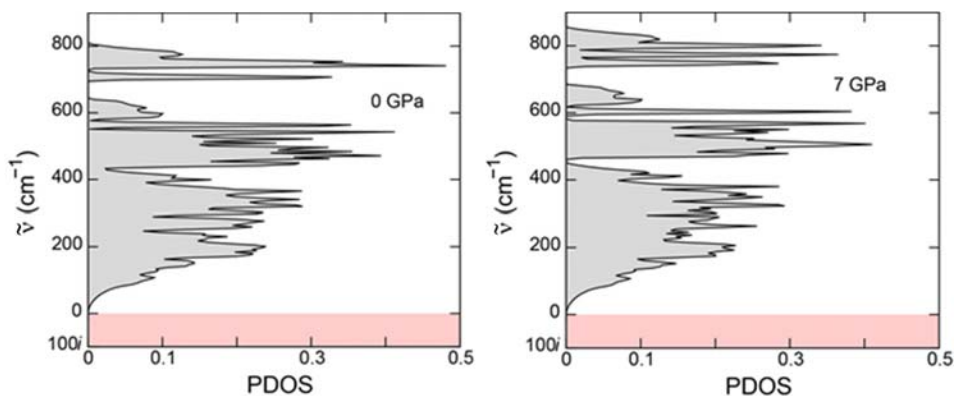


**Figure 2.** Calculated phonon density of states (PDOS) of HP-MoO<sub>2</sub> at ambient pressure (left) and slightly above the calculated transition pressure (right).

The phase purity of the  $\alpha$ -MoO<sub>2</sub> starting material was verified using powder XRD on the PANalytical X'Pert MPD Pro. No detectable amounts of MoO<sub>3</sub>, suboxides, or elemental molybdenum were found in the precursor for the high-pressure experiments. Optical analysis of the products in reflected light revealed that they consist of a powder-like opaque phase (about 1–4  $\mu\text{m}$  in size), in which additionally some larger crystals 50–100  $\mu\text{m}$  in size occurred; the latter were picked for the single-crystal diffraction experiment, as we discuss below. Several powder X-ray diffraction patterns of the high-pressure product were measured using the Rigaku diffractometer from different portions of the specimen using different preparation strategies. The diffraction patterns taken do not differ in the number and the positions of the reflections, but only in the relative intensities.

All recorded patterns are characterized by sharp reflections and a high background with a maximum at  $2\theta \approx 22.5^\circ$ . A first phase analysis revealed a close structural relationship to HP-WO<sub>2</sub>.<sup>29</sup> Although an *ab-initio* structure solution from powder data was unsuccessful, Le Bail whole pattern fitting<sup>33</sup> results in a good accordance of experimental and calculated data. From the different preparation methods, the best results came from a portion of the sample which we had grounded for 5 min, mounted on a CryoLoop (Hampton Research), and rotated during the data acquisition of 30 minutes at a speed of 3°/s over 360°. The diffraction pattern of this portion is depicted in **Figure 3** with the results of the Le Bail fit in the range  $10^\circ < 2\theta < 120^\circ$ .

The problems occurring during Rietveld refinement using a distinct structure model may indicate the presence of multiple preferred orientations of the crystallites. The small amount of substance used for powder diffraction consists of few and relatively large crystallites. This does not comply with the requirements for powder XRD, where a high number of small crystallites with a statistical size distribution is essential. Therefore, the observed intensity deviations of measured and calculated patterns are significant and the presented diffractogram is unbiased. A solution for this problem might be a synthesis at lower pressures above the transition pressure, so that a regular powder is formed.



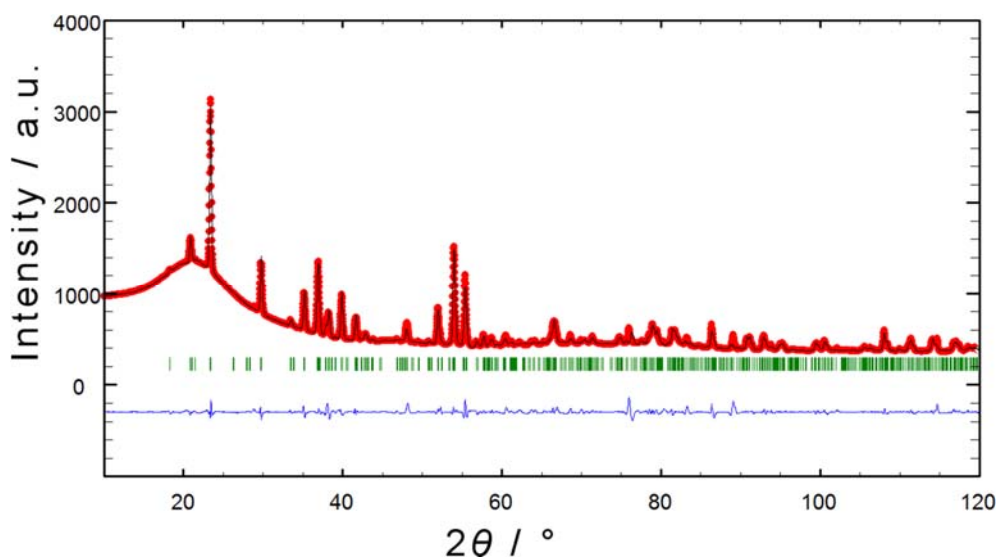


**Figure 3.** X-ray powder diffraction pattern (Cu  $K_{\alpha}$  radiation) of HP-MoO<sub>2</sub> with the results of the Le Bail profile fit (red: measured; black: calculated; green: Bragg-reflection positions; blue: difference plot).

However, it was possible to isolate a small violet prism with a size of  $0.057 \times 0.067 \times 0.086$  mm<sup>3</sup> fit for single crystal-diffraction (see **Figure S1**). Crystallographic details are summarized in **Table 1**. Laue-group determination was unambiguous; the centrosymmetric space-group type *Pnma* was chosen over *Pn2<sub>1</sub>a* for reasons of intensity statistics and commonness. Structure solution using Direct Methods proceeded without problems and yielded the cation positions. Anion positions were deduced from maxima of a difference Fourier map. Refinement proceeded smoothly with an accurate absorption correction and the application of an extinction correction parameter as crucial aspects.

**Table 1.** Results of the single-crystal analysis and Le Bail decomposition of HP-MoO<sub>2</sub>.

	Single-crystal	Powder (Le Bail)
$\lambda$ / pm	154.184	154.060, 154.443
Structure type		HP-WO <sub>2</sub>
Crystal system		orthorhombic
Space group		<i>Pnma</i> (No. 62)
<i>Z</i>		12
Crystal size / mm <sup>3</sup>	0.057 × 0.067 × 0.086	–
<i>a</i> / pm	969.21(3)	971.62(7)
<i>b</i> / pm	843.22(3)	845.73(6)
<i>c</i> / pm	471.88(2)	475.10(4)
<i>V</i> / 10 <sup>6</sup> pm <sup>3</sup>	385.65(2)	390.40(5)
$\rho_{\text{calc}}$ / g·cm <sup>-3</sup>	6.61	6.53
$\mu$ / mm <sup>-1</sup>	78.4	–
$2\theta_{\text{max}}$ / °	73.366	120.000
$h_{\text{min}}, h_{\text{max}}$	–11, 10	0, 10
$k_{\text{min}}, k_{\text{max}}$	–10, 9	0, 9
$l_{\text{min}}, l_{\text{max}}$	–5, 5	0, 5
$T_{\text{min}}, T_{\text{max}}$	0.020, 0.162	–
Measured reflections	1931	632
Independent reflections ( $R_{\text{int}}$ )	403 (0.0276)	316
Observed <sup>a</sup> reflections ( $R_{\sigma}$ )	393 (0.0122)	–
Data, restraints, parameters	403, 0, 47	6516, 0, 45
$R_1$   $R_F$	0.0267	0.0310
$wR_2^b$   $R_{\text{Bragg}}$	0.0700	0.0354
$R_{\text{wp}}$	–	0.0280
$R_{\text{exp}}$	–	0.0404
$u^b, v^b$	0.0507	–
<i>S</i>	1.157	0.692
$\rho_e(\text{min, max}) / 10^{-6} \text{ pm}^{-3}$	–1.57, 1.29	–

a:  $I > 2\sigma(I)$ .

b:  $w = 1/[\sigma^2(F_o^2) + (uP)^2 + vP]$ ;  $P = [\max(F_o^2, 0) + 2F_c^2]/3$

HP-MoO<sub>2</sub> crystallizes isotypically to HP-WO<sub>2</sub> in the orthorhombic crystal system in space group *Pnma* (No. 62) with 12 formula units per unit cell. As expected, the calculated density of the new high-pressure polymorph (6.61 g·cm<sup>-3</sup>) is slightly higher in comparison to monoclinic  $\alpha$ -MoO<sub>2</sub> (6.46 g·cm<sup>-3</sup>).<sup>4</sup> The crystal structure is built of layers of oxide and molybdenum ions alternating along the *c* axis (**Figure 4, left**). The oxide layers can be described as an almost hexagonal close packing with the metal atoms occupying one half of the octahedral sites. The coordination number of the metal ions is six and therefore not increased with respect to  $\alpha$ -MoO<sub>2</sub>. Oxide ions are surrounded by three molybdenum ions and do not form perfectly ordered layers, thereby preventing an ideal packing. The distorted MoO<sub>6</sub> octahedra are connected over two edges forming zig-zag chains along the *b* axis. Those chains form alternating layers along the *c* axis (indicated as red and yellow polyhedra). Inside one layer, the chains are separated by tunnels but share vertices with chains of neighboring layers *via* O1, O2, and O3 (**Figure 4, right**). One characteristic element of the chains is the sequence of –Mo2–Mo1–Mo2– polyhedra with Mo1 polyhedra as the turning point of the zig-zag chains (**Figure 5**). This is possible because the polyhedra around Mo1 are linked over *cis*-positioned edges, while the Mo2 polyhedra are linked *via* edges in *trans* position. All three polyhedra in one sequence are connected *via* O4. This connection extends into the tunnel, which leads to a tothing of the layers. Additionally, the Mo2 polyhedra are connected to the Mo1 polyhedra *via* O1 and to the other Mo2 polyhedra *via* O3. The –Mo2–Mo1–Mo2– chains are linked among each other *via* the O2 ions of the Mo2 polyhedra.

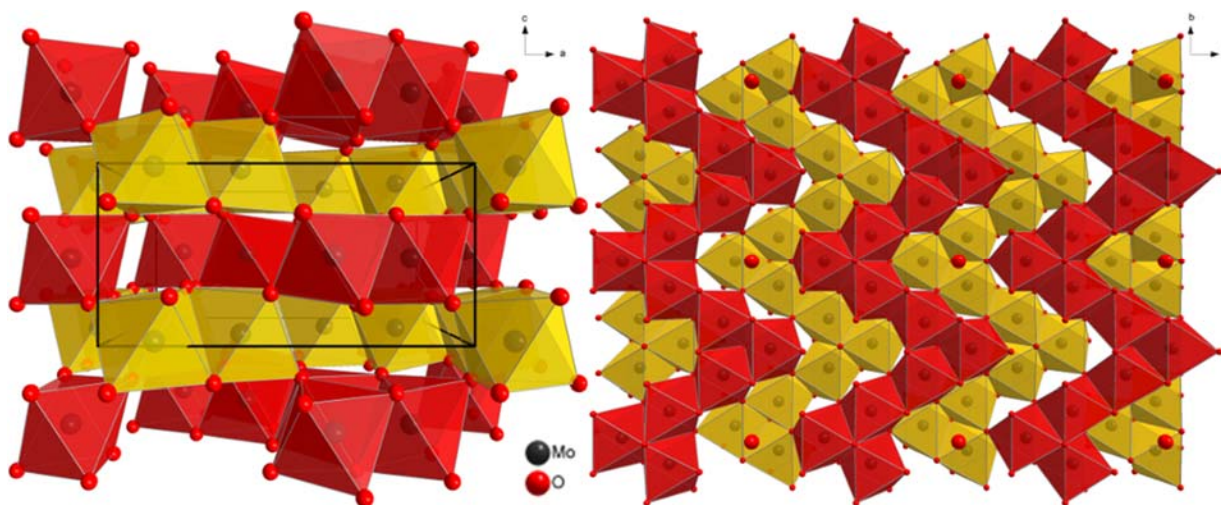


**Figure 4.** Crystal structure of HP-MoO<sub>2</sub>. Left: layer-like structure along *c* axis with unit cell; right: arrangement of the zig-zag chains of two layers. Red and yellow polyhedra indicate different layers. Unbound oxide ions indicate the tootching of the layers.

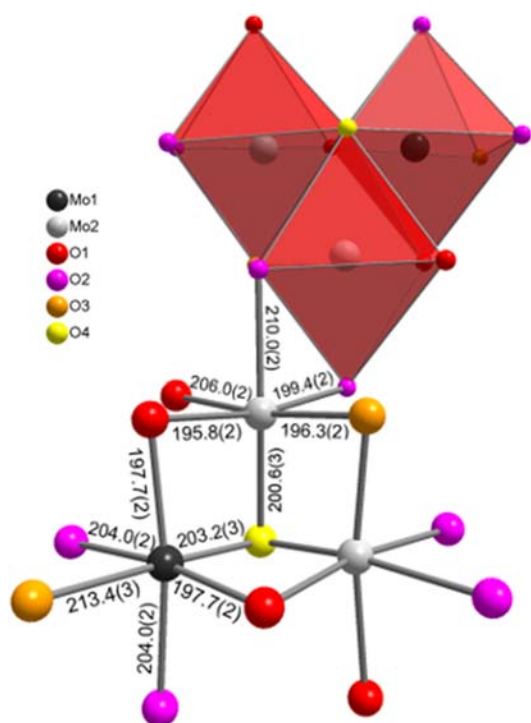


**Figure 5.** Coordination polyhedra and connectivity of the atoms inside one zig-zag chain with bond lengths (in pm).

According to the atomic parameters in **Table 2**, all oxide ions are located very close to a glide plane. Additionally, O3 and O4 are located on a mirror plane. The seemingly differing atomic positions in the original HP-WO<sub>2</sub> publication can be resolved by inverting the *c* axis (*i.e.*, mirroring the atoms at the basal *ab* plane).<sup>29</sup> **Figure 5** also depicts the corresponding Mo–O bond lengths. The average bond length of 203.3 pm for the (Mo1)O<sub>6</sub> polyhedron and 201.4 pm for the (Mo2)O<sub>6</sub> polyhedron are in good agreement with the ionic radii of both elements (65 pm for Mo<sup>4+</sup> in a 6-fold coordination and 136 pm for O<sup>2-</sup> in a 3-fold coordination).<sup>48</sup> Molybdenum ions are at least 251.60(5) pm apart from each other. Details about distances and angles can be found in the crystallographic information file (CIF) in the **Supporting Information**.

The almost regular hcp arrangement of the oxide anions in HP-MoO<sub>2</sub> and the ordered molybdenum positions readily call for a close group theoretical relationship starting from the NiAs structure as aristotype where the octahedral voids of the arsenic substructure are completely filled.

The corresponding group-subgroup scheme in the Bärnighausen formalism<sup>49-51</sup> is presented in **Figure 6**. We start with space group P6<sub>3</sub>/mnc (both hcp and NiAs), and the first symmetry reduction goes to space group Cmc<sub>m</sub> via a translationengleiche transition of index 3 (t3), leading to the orthohexagonal setting. The following decentering of the lattice (klassengleiche transition of index 2 (k2) to Pmmn) leads to a first splitting of the oxygen site. The unit cell is then enlarged by another klassengleiche transition of index 2 (k2) to Pnma followed by an isomorphic transition to Pnma upon tripling the b parameter. Of the four crystallographically independent molybdenum sites only two are occupied in an ordered manner; two remain empty. Comparison of the calculated and refined positional parameters (**Table 2**) show the most pronounced deviation for the *z* parameter of the O4 atoms (connecting three polyhedra). All other atoms show smaller shifts from the subcell sites. These are all consequence of the molybdenum ordering.

**Table 2.** Experimental and computed (DFT with D3 dispersion correction) atomic parameters of the new high-pressure polymorph of MoO<sub>2</sub>.

<b>Atom</b>		<b>Wyckoff</b>	<b><i>x</i></b>	<b><i>y</i></b>	<b><i>z</i></b>
Mo1	(Exp.)	4 <i>c</i>	0.36523(5)	¼	0.02048(10)
	(DFT-D3)		0.3638	¼	0.0201
Mo2	(Exp.)	8 <i>d</i>	0.13305(4)	0.10081(4)	0.00614(5)
	(DFT-D3)		0.1326	0.1015	0.0077
O1	(Exp.)	8 <i>d</i>	0.20010(2)	0.57460(2)	0.27710(5)
	(DFT-D3)		0.2001	0.5740	0.2757
O2	(Exp.)	8 <i>d</i>	0.45670(2)	0.08630(2)	0.27760(5)
	(DFT-D3)		0.4559	0.0867	0.2764
O3	(Exp.)	4 <i>c</i>	0.04340(3)	¼	0.74520(7)
	(DFT-D3)		0.0418	¼	0.7429
O4	(Exp.)	4 <i>c</i>	0.20630(3)	¼	0.30120(7)
	(DFT-D3)		0.2054	¼	0.3034

The calculated HP-MoO<sub>2</sub> structural parameters are in excellent agreement with the experimentally observed results: **Table 3** lists the cell parameters obtained from the experiment compared to the calculated results. The DFT-D3 results nicely corroborates the experiment, while the exclusion of the dispersion correction leads to a slight overestimation of the cell parameters. When comparing the calculated and measured spatial parameters the observation remains the same, the theory (DFT-D3) being in nice accord with the experiment. To quantify the conformity, we calculated the root mean square (RMS)<sup>49</sup> between the experimental and calculated atomic positions, and the absolute RMS = 1.2 pm confirms an excellent agreement.

**Table 3.** Comparison of experimental and DFT calculated cell parameters (pm) with and without D3 dispersion correction.

	<b>Exp.</b>	<b>DFT(D3)</b>	<b>DFT</b>
<i>a</i>	969.2	971.2	975.5
<i>b</i>	843.2	847.7	850.8
<i>c</i>	471.9	476.2	482.4

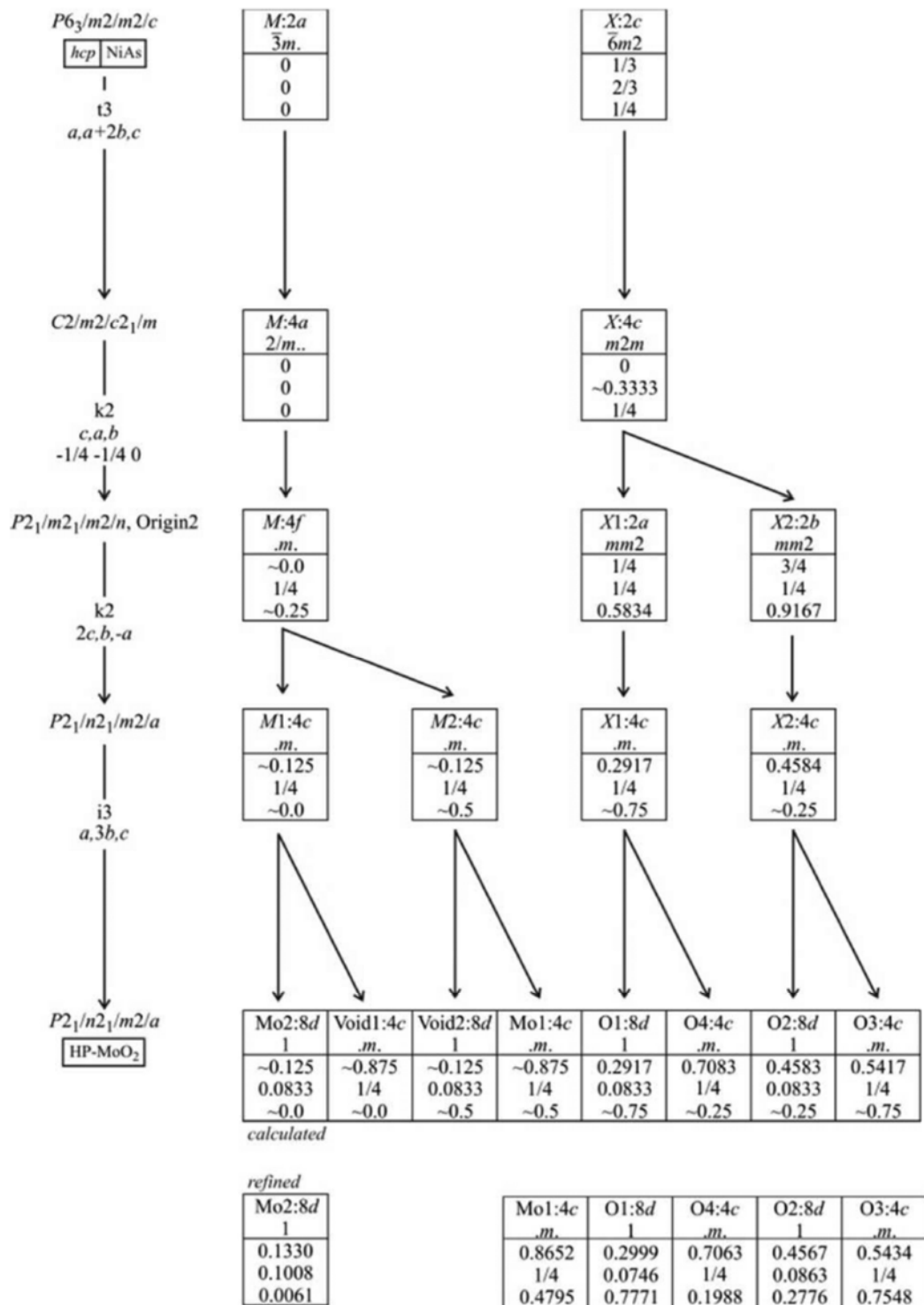


**Figure 6.** Group-subgroup scheme (Bärnighausen formalism) for the group-theoretical relationship between the NiAs structure (aristotype) and the crystal structure of HP-MoO<sub>2</sub>.

Even when starting with large local magnetic moments, spin-polarized electronic-structure calculations using either ferromagnetic (FM) or antiferromagnetic (AFM) orderings immediately converged into non-magnetic states with identical total energies. It is therefore safe to assume either diamagnetic behavior or weak metallic paramagnetism without local moments. This is quite understandable by comparing HP-MoO<sub>2</sub> with the ferromagnetic, lighter homologue CrO<sub>2</sub>. In HP-MoO<sub>2</sub>, the two leftover 4*d* electrons of Mo(IV) are well shielded by the filled internal 3*d* shell and, because the exchange splitting, which is responsible for spin polarization, scales with the effective nuclear charge, the exchange splitting in HP-MoO<sub>2</sub> is insufficient. The calculated electronic DOS of HP-MoO<sub>2</sub> shows only very few states at the Fermi level, suggesting either a minute overlap between valence and conduction band (*i.e.*, a bad metal) or a semiconductor with a zero band gap, as shown in **Figure 7**. We therefore tentatively suggest HP-MoO<sub>2</sub> as a semimetal with a low electrical conductivity.

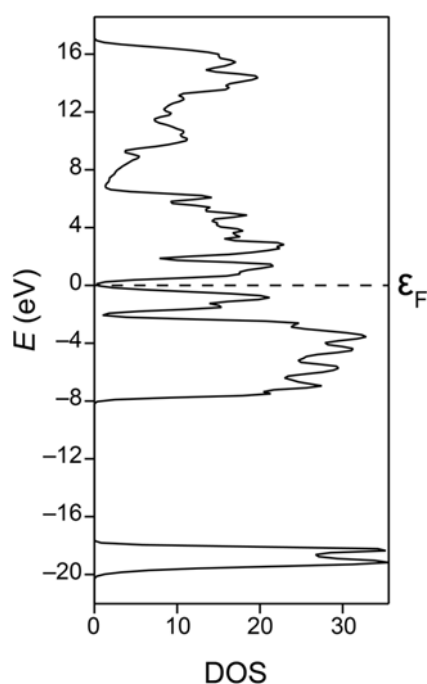


**Figure 7.** Calculated electronic density of states (DOS) of HP-MoO<sub>2</sub>. The minute overlap between the valence and conduction band at the Fermi level classifies the compound as a semimetal.



As for the vibrational properties, we show the recorded Raman spectrum of HP-MoO<sub>2</sub> in **Figure 8**. According to group theory, a total sum of  $\Gamma = 15 A_g + 12B_{1g} + 15 B_{2g} + 12B_{3g}$  first-order Raman-active modes is expected for HP-MoO<sub>2</sub>. We could observe 26 Raman-related features; the detailed Raman mode list and a tentative mode-symmetry assignment are given in the **Supplement**. In agreement with the calculated phonon DOS (**Figure 2**), the spectrum can be divided in three wavenumber regions: 100–420 cm<sup>-1</sup>, 420–650 cm<sup>-1</sup>, and 700–850 cm<sup>-1</sup>. To the best of our knowledge, this is the first report of the Raman response of a HP-WO<sub>2</sub>-type structure. Consequently, our Raman spectra can serve as a basis for the (micro) identification of this phase.

Regarding the vibration-specific Raman-mode assignments on the other hand, we do not have a reference Raman spectrum for direct comparison. Nevertheless, we can draw some analogies from the Raman mode assignment of the starting material, the monoclinic  $\alpha$ -MoO<sub>2</sub> phase.<sup>50</sup> Therefore, we can assign the 100–420 cm<sup>-1</sup>, 420–650 cm<sup>-1</sup>, and 700–850 cm<sup>-1</sup> regions to external vibrations (*e.g.*, translations of the MoO<sub>6</sub> units), and to the Mo–O–Mo bending and Mo–O stretching modes, respectively.

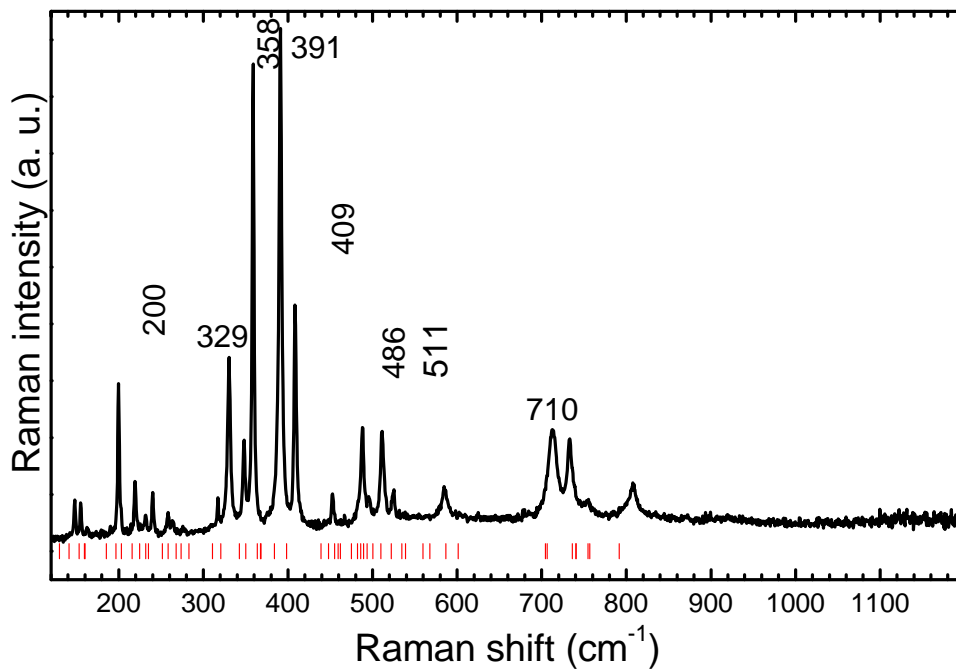


**Figure 8.** Raman spectrum of HP-MoO<sub>2</sub> at ambient conditions ( $\lambda = 514.5$  nm). The red tick symbols represent the calculated Raman-mode wavenumbers (**Supplement**).

**Figure 9** shows the temperature dependence of the molar magnetic susceptibility ( $\chi$ ) of the HP-MoO<sub>2</sub> sample measured at 10 kOe; the data obtained at 50 kOe coincides with the 10 kOe data and is therefore not shown. In order to isolate the contribution of the sample, the  $\chi$  data was corrected by subtracting the susceptibility of an empty PE capsule. The sample shows almost temperature-independent diamagnetic behavior within the whole temperature range. The susceptibility at 300 K exhibits a value of  $-1.1(1) \cdot 10^{-6} \text{ emu} \cdot \text{mol}^{-1}$ . Due to the small sample mass available for this measurement, the relative error of the susceptibility  $\chi(300 \text{ K})$  was estimated to be 10%. The observed diamagnetism is in line with the absence of any localized electron at the Mo<sup>4+</sup> cation. The values of the observed susceptibilities are about one order of magnitude smaller compared to the calculated ones ( $-41 \cdot 10^{-6} \text{ emu} \cdot \text{mol}^{-1}$ ) using the diamagnetic increments ( $\chi(\text{Mo}^{4+}) = -17 \cdot 10^{-6} \text{ emu} \cdot \text{mol}^{-1}$ ;  $\chi(\text{O}^{2-}) = -12 \cdot 10^{-6} \text{ emu} \cdot \text{mol}^{-1}$ ) listed in Ref. <sup>51</sup>. They are, however, in accord with the outcome of computation (*vide supra*).

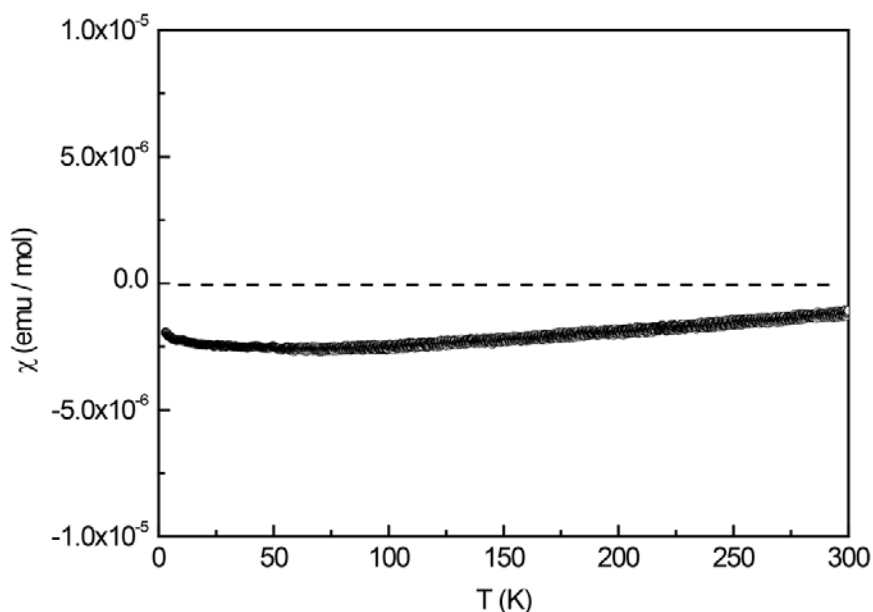


**Figure 9.** Temperature-dependent molar magnetic susceptibility  $\chi$  of HP-MoO<sub>2</sub>, measured with a magnetic field strength of 10 kOe.

## Conclusion

A new high-pressure polymorph of MoO<sub>2</sub> was synthesized using a multi-anvil press at 18 GPa and 1073 K. Leaving  $\alpha$ -MoO<sub>2</sub> for 30 h under these  $p$  and  $T$  conditions we transformed the

powdered material into single crystals, the structure of which was then determined by means of X-ray diffraction. Measurements of the magnetic susceptibility show a diamagnetic behavior. The obtained experimental data are in excellent agreement with our computed results. As the calculations predict an additional phase transition to an *ortho*-TiO<sub>2</sub>-type structure at higher pressures (~28 GPa), further experiments are in the focus of our interest. In general, taking into consideration the straight synthesis of HP-MoO<sub>2</sub>, it seems to be worth the efforts extending the work also to other binary transition metal oxides.

## Acknowledgments

This work was supported by the Deutsche Forschungsgemeinschaft (DFG) within the priority program SPP 1415 (LE 781/11-2, DR 342/22-2). We thank Reiner Schulz and Andreas Ebert for technical support during the high-pressure experiments and Hans-Peter Nabein for the help with the powder diffraction measurements. Single-crystal diffraction measurements by Paula Nixdorf are gratefully acknowledged.

## References

- (1) Goldschmidt, V. M.; Barth, T.; Holmsen, D.; Lunde, G.; Zachariasen, W. *Skr. Utg. av det Nor. Videnskaps-Akademi i Oslo I Mat. Klasse* **1926**, 5–21.
- (2) Magnéli, A.; Andersson, G.; Blomberg, B.; Kihlberg, L. *Anal. Chem.* **1952**, 24 (12), 1998–2000.
- (3) Magnéli, A.; Andersson, G.; Sundkvist, G. *Acta Chem. Scand.* **1955**, 9, 1378–1381.
- (4) Brandt, B. G.; Skapski, A. C. *Acta Chem. Scand.* **1967**, 21, 661–672.
- (5) Rogers, D. B.; Shannon, R. D.; Sleight, A. W.; Gillson, J. L. *Inorg. Chem.* **1969**, 8 (4), 841–849.
- (6) Eyert, V.; Horny, R.; Höck, K.-H.; Horn, S. *J. Phys. Condens. Matter* **2000**, 12 (23), 4923–

4946.

- (7) Seisenbaeva, G. A.; Sundberg, M.; Nygren, M.; Dubrovinsky, L.; Kessler, V. G. *Mater. Chem. Phys.* **2004**, *87* (1), 142–148.
- (8) Becker, N.; Dronskowski, R. *J. Solid State Chem.* **2016**, *237*, 404–410.
- (9) Sasaki, T. A.; Kiuchi, K. *Chem. Phys. Lett.* **1981**, *84* (2), 356–360.
- (10) Sasaki, T. A.; Soga, T.; Adachi, H. *Phys. Status Solidi B* **1982**, *113* (2), 647–655.
- (11) Burdett, J. K. *Inorg. Chem.* **1985**, *24* (14), 2244–2253.
- (12) Yoshino, H.; Shimokoshi, K.; Miyazaki, E. *J. Electron Spectros. Relat. Phenomena* **1985**, *36* (3), 269–279.
- (13) Scanlon, D. O.; Watson, G. W.; Payne, D. J.; Atkinson, G. R.; Egdell, R. G.; Law, D. S. L. *J. Phys. Chem. C* **2010**, *114* (10), 4636–4645.
- (14) Kruglova, A. G. *Int. Geol. Rev.* **1982**, *24* (5), 617–620.
- (15) Shi, Y.; Guo, B.; Corr, S. A.; Shi, Q.; Hu, Y.-S.; Heier, K. R.; Chen, L.; Seshadri, R.; Stucky, G. D. *Nano Lett.* **2009**, *9* (12), 4215–4220.
- (16) Camacho-López, M. A.; Escobar-Alarcón, L.; Picquart, M.; Arroyo, R.; Córdoba, G.; Haro-Poniatowski, E. *Opt. Mater. (Amst)*. **2011**, *33* (3), 480–484.
- (17) Auburn, J. J.; Barberio, Y. L. *J. Electrochem. Soc.* **1987**, *134* (3), 638.
- (18) Liang, Y.; Yang, S.; Yi, Z.; Lei, X.; Sun, J.; Zhou, Y. *Mater. Sci. Eng. B* **2005**, *121* (1–2), 152–155.
- (19) Yang, L. C.; Gao, Q. S.; Tang, Y.; Wu, Y. P.; Holze, R. *J. Power Sources* **2008**, *179* (1), 357–360.
- (20) Sun, Y.; Hu, X.; Luo, W.; Huang, Y. *ACS Nano* **2011**, *5* (9), 7100–7107.
- (21) Liang, Y.; Yi, Z.; Yang, S.; Zhou, L.; Sun, J.; Zhou, Y. *Solid State Ionics* **2006**, *177* (5–6), 501–505.

- (22) Ma, Y.-R.; Tsai, C.-C.; Lee, S. F.; Cheng, K.-W.; Liou, Y.; Yao, Y. D. *J. Magn. Magn. Mater.* **2006**, *304* (1), e13–e15.
- (23) Liu, X.; He, Y.; Wang, S.; Zhang, Q. *J. Alloys Compd.* **2011**, *509* (SUPPL. 1), S408–S411.
- (24) Bueno-Core, G. E.; Cabello, G.; Klahn, A. H.; Lucero, A.; Nuñez, M. V.; Torrejón, B.; Castillo, C. *Polyhedron* **2010**, *29* (6), 1551–1554.
- (25) Hu, B.; Mai, L.; Chen, W.; Yang, F. *ACS Nano* **2009**, *3* (2), 478–482.
- (26) Haines, J.; Léger, J. M.; Hull, S.; Petitet, J. P.; Pereira, A. S.; Perottoni, C. A.; Jornada, J. A. H. *J. Am. Ceram. Soc.* **2005**, *80* (7), 1910–1914.
- (27) Fu, Z.; Liang, Y.; Wang, S.; Zhong, Z. *Phys. Status Solidi B* **2013**, *250* (10), 2206–2214.
- (28) Woodhead, K.; Pascarelli, S.; Hector, A. L.; Briggs, R.; Alderman, N.; McMillan, P. F. *Dalt. Trans.* **2014**, *43* (25), 9647–9654.
- (29) Sundberg, M.; Werner, P.-E.; Zibrov, I. P. *Z. Krist.* **1994**, *209* (8), 662–666.
- (30) McCarron, E. M.; Calabrese, J. C. *J. Solid State Chem.* **1991**, *91* (1), 121–125.
- (31) Koch-Muller, M.; Mugnaioli, E.; Rhede, D.; Speziale, S.; Kolb, U.; Wirth, R. *Am. Mineral.* **2014**, *99* (11–12), 2405–2415.
- (32) Rietveld, H. M. *Acta Crystallogr.* **1967**, *22* (1), 151–152.
- (33) Le Bail, A.; Duroy, H.; Fourquet, J. L. *Mater. Res. Bull.* **1988**, *23* (3), 447–452.
- (34) Rodríguez-Carvajal, J. In *Abstracts of the Satellite Meeting on Powder Diffraction of the XV IUCr Congress*; 1990; p 127.
- (35) Rigaku Oxford Diffraction. Rigaku Corporation: Oxford (U.K.) 2015.
- (36) Clark, R. C.; Reid, J. S. *Acta Crystallogr., Sect. A Found. Crystallogr.* **1995**, *51* (6), 887–897.
- (37) Sheldrick, G. M. *Acta Crystallogr., Sect. C Struct. Chem.* **2015**, *71* (1), 3–8.
- (38) Brandenburg, K. Crystal Impac GbR: Bonn (Germany), 2015 2012.

- (39) Kresse, G.; Furthmüller, J. *Comput. Mater. Sci.* **1996**, *6* (1), 15–50.
- (40) Blöchl, P. E. *Phys. Rev. B* **1994**, *50* (24), 17953–17979.
- (41) Perdew, J. P.; Burke, K.; Ernzerhof, M. *Phys. Rev. Lett.* **1996**, *77* (18), 3865–3868.
- (42) Perdew, J. P.; Burke, K.; Ernzerhof, M. *Phys. Rev. Lett.* **1997**, *78* (7), 1396–1396.
- (43) Grimme, S.; Antony, J.; Ehrlich, S.; Krieg, H. *J. Chem. Phys.* **2010**, *132* (15), 154104.
- (44) Grimme, S.; Ehrlich, S.; Goerigk, L. *J. Comput. Chem.* **2011**, *32* (7), 1456–1465.
- (45) Birch, F. *Phys. Rev.* **1947**, *71* (11), 809–824.
- (46) Togo, A.; Oba, F.; Tanaka, I. *Phys. Rev. B* **2008**, *78* (13), 134106.
- (47) Stoffel, R. P.; Wessel, C.; Lumey, M.-W.; Dronskowski, R. *Angew. Chemie Int. Ed.* **2010**, *49* (31), 5242–5266.
- (48) Shannon, R. D. *Acta Crystallogr. Sect. A* **1976**, *32* (5), 751–767.
- (49) Bärnighausen, H. *MATCH Commun. Math. Comput. Chem.* **1980**, *9*, 139-175.
- (50) Müller, U. *Z. Anorg. Allg. Chem.* **2004**, *630*, 1519-1537.
- (51) Müller, U. *Symmetriebeziehungen zwischen verwandten Kristallstrukturen*, 1st ed.; Vieweg + Teubner Verlag: Wiesbaden, 2012.
- (52) George, J.; Deringer, V. L.; Dronskowski, R. *Inorg. Chem.* **2015**, *54* (3), 956–962.
- (53) Dieterle, M.; Mestl, G. *Phys. Chem. Chem. Phys.* **2002**, *4* (5), 822–826.
- (54) Bain, G. A.; Berry, J. F. *J. Chem. Educ.* **2008**, *85* (4), 532.

## SUPPLEMENT

**Table S1:** Assignments, calculated and experimental wavenumbers for the HP-MoO<sub>2</sub> Raman-active modes. The letters in parenthesis indicate the respective relative band intensities: w = weak, vw = very weak, s = strong, vs = very strong, sh = shoulder. The matching between the calculated and experimental Raman mode wavenumbers is tentative.

<b>HP-MoO<sub>2</sub> Raman-active mode wavenumbers (cm<sup>-1</sup>)</b>		
Assignment	Calculated	Observed
B <sub>3g</sub>	129.80	
A <sub>g</sub>	141.29	148 (w)
A <sub>g</sub>	153.08	155 (w)
B <sub>3g</sub>	159.51	
B <sub>1g</sub>	160.07	163 (vw)
B <sub>2g</sub>	185.33	
A <sub>g</sub>	196.64	200 (s)
B <sub>1g</sub>	203.03	
B <sub>2g</sub>	215.79	219 (w)
B <sub>1g</sub>	224.89	
B <sub>3g</sub>	232.08	232 (vw)
B <sub>2g</sub>	234.88	240 (w)
B <sub>2g</sub>	251.61	
A <sub>g</sub>	258.15	258 (w)
B <sub>3g</sub>	267.83	264 (w)
B <sub>1g</sub>	273.81	276 (vw)
B <sub>1g</sub>	282.81	
B <sub>2g</sub>	310.76	317 (vw)
A <sub>g</sub>	320.73	330 (s)
B <sub>2g</sub>	342.45	348 (w)
A <sub>g</sub>	349.92	359 (s)
B <sub>3g</sub>	350.10	
B <sub>2g</sub>	363.70	

B <sub>3g</sub>	367.56	
B <sub>1g</sub>	368.11	
A <sub>g</sub>	383.93	391 (vs)
A <sub>g</sub>	398.21	409 (s)
B <sub>2g</sub>	439.17	
B <sub>3g</sub>	448.01	
B <sub>1g</sub>	455.00	453 (w)
B <sub>1g</sub>	459.25	
B <sub>3g</sub>	462.14	
B <sub>2g</sub>	474.82	
A <sub>g</sub>	482.10	488 (s)
B <sub>2g</sub>	485.82	
B <sub>3g</sub>	489.35	496 (vw)
B <sub>1g</sub>	493.35	
A <sub>g</sub>	500.28	511 (s)
B <sub>2g</sub>	510.00	
A <sub>g</sub>	522.31	525 (w)
B <sub>3g</sub>	534.59	
B <sub>1g</sub>	539.13	
B <sub>3g</sub>	559.50	
B <sub>1g</sub>	567.82	585 (w)
A <sub>g</sub>	586.64	
B <sub>2g</sub>	601.32	
A <sub>g</sub>	704.32	713 (s)
B <sub>2g</sub>	706.23	
A <sub>g</sub>	736.34	733 (s)
B <sub>1g</sub>	740.22	
B <sub>2g</sub>	740.73	
A <sub>g</sub>	754.79	753 (sh)
B <sub>3g</sub>	756.84	
B <sub>2g</sub>	791.66	807 (w)

---